ACS OMEGA

Open Access

http://pubs.acs.org/journal/acsodf

Article

Magnetic Chitosan Nanocomposites Derived from Industrial Solid Waste: A Promising Approach for Arsenic(III) Remediation

Le Minh Tri, Pham Thi Mai Huong, and Nguyen Thi Huong*

Cite This: *ACS Omega* 2025, 10, 3351−3360

Read Online

ACCESS | Metrics & More | Article Recommendations | Supporting Information

ABSTRACT: In this paper, the "waste to adsorbent" strategy was proposed to synthesize Fe_3O_4 nanoparticles using the ultrasonic-assisted coprecipitation method from Bayer industrial waste. The nanoparticles were combined with chitosan (CS) to enhance their physicochemical properties. The well-covered CS on the surface of Fe_3O_4 is characterized by the nanocomposite's saturation magnetization of 50.2 emu/g, zeta potential of −14.2 mV, and specific surface area of 93.64 m^2/g. The highest percentage removal efficiency was 96.73% at pH 4, with the adsorbent dosage of 0.5 g/L and the As(III) concentration of 10 mg/L, which suggests that the material is an ideal adsorbent for arsenic(III) remediation. Furthermore, the effects, kinetics, isotherms, and thermodynamic study of the As(III) adsorption process in an aqueous solution of Fe_3O_4/CS nanocomposites were thoroughly investigated.

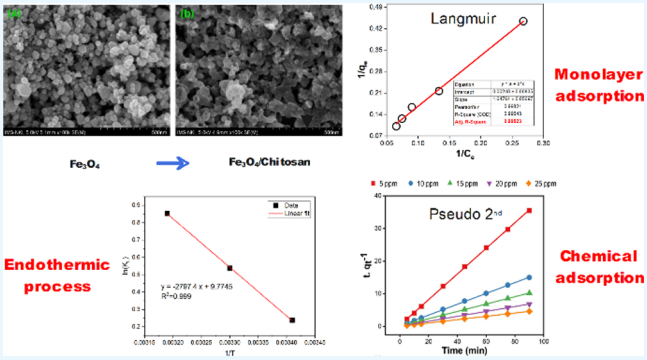

1. INTRODUCTION

The development of heavy industry is an important part of the industrialization process of a country, especially for developing nations. Heavy industry typically includes large-scale manufacturing sectors such as steel production, cement, chemicals, and other related industries. Throughout history, the development of heavy industry has contributed to economic growth and created a solid infrastructure foundation for developing economies. However, the development of the heavy industry also comes with many serious environmental issues. Environmental pollution from factories, manufacturing plants, and extraction activities can have significant negative impacts on the environment and human health.[1]

One such environmental issue is the contamination of water and soil by arsenic.[2] Arsenic is a naturally occurring element present in the Earth's crust in various forms, with inorganic arsenic being the most dangerous. Its toxicity has been well-documented, and exposure to arsenic poses significant health risks. This element can accumulate in crops such as rice, vegetables, and seafood, further exacerbating the issue.[3] Industrial activities, particularly the use of arsenic in pesticides and wood preservatives, contribute to its release into the environment. Acute ingestion of high levels of arsenic can result in severe symptoms, such as nausea, vomiting, diarrhea, abdominal pain, and shock. Most environmental arsenic contamination stems from human activities, causing life-threatening complications for millions of people who consume water and food from arsenic-contaminated sources.[4]

Various strategies have been explored for the removal of arsenic in wastewater, including photocatalysis,[5] microbial decomposition,[6] reverse osmosis,[7] membrane filtration,[8] ion exchange,[9] and adsorption.[10] Adsorption is particularly advantageous due to its ease of operation, affordability, environmental sustainability, and fast processing capabilities. As a result, a wide range of solid adsorbents have been engineered for wastewater treatment, including covalent organic frameworks, metal−organic frameworks,[11] organic polymers,[12] porous inorganic materials,[13] and metal oxide materials.[14] Iron oxides, in particular, are renowned for their high capacity to adsorb arsenic and are extensively applied in real-world scenarios.[15] Nonetheless, conventional methods for synthesizing iron oxides, such as solvothermal and hydrothermal techniques,[16] require high temperatures and pressures, use toxic solvents, and consume significant amounts of energy. Thus, the development of highly active iron oxide-based adsorbents using ecofriendly and efficient methodologies presents a significant challenge.

In Vietnam, a notable discovery is that the byproducts from the Bayer process used to refine bauxite ore into Al_2O_3 contain significant amounts of metal oxides, including Fe_2O_3, Al_2O_3, CaO, SiO_2, and TiO_2, with iron oxide comprising up to 60%. Additionally, this highly alkaline waste material, with a pH

Received: July 2, 2024
Revised: January 9, 2025
Accepted: January 16, 2025
Published: January 24, 2025

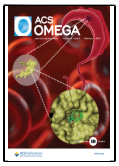

Scheme 1. Synthesis of the Fe_3O_4/CS Nanocomposite

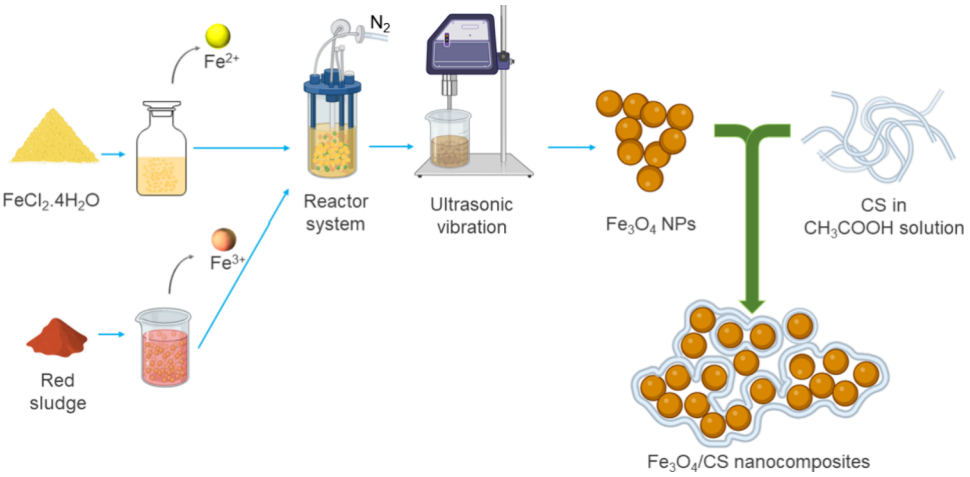

between 11 and 12, contributes to severe environmental pollution and poses substantial health risks to the local population. Consequently, there is a strong incentive to recycle this harmful industrial solid waste and transform it into valuable adsorbents.[17]

Since 2017, the adsorption of As (III) in red mud aqueous solution has been investigated by researchers after the separation of aluminum and alkali-soluble components.[18] Three years later, in 2020, the ferromagnetic nanoparticles were successfully fabricated and tested for Cr (VI) adsorption.[19] However, with a focus on enhancing the efficiency and characteristics of the material, research has been continuously conducted on its nano surfaces to not only improve diffusion but also reduce particle agglomeration and promote its recovery rates.

In this study, chitosan (CS) has been selected as an agent for the modification of ferromagnetic nanoparticles owing to its antibacterial properties, biodegradability, and other favorable characteristics. These include abundant sources allowing for low-cost and large-scale production,[20] chemical stability when combined with Fe_3O_4,[21] as well as good biocompatibility,[22] rendering it suitable for applications such as catalyst supports and biomedical materials. Furthermore, its strong ion exchange properties facilitate the rapid removal of heavy metals and contribute to its high adsorption capacity.[23] The adsorption of heavy metals is attributed to ion exchange, complexation, and electrostatic interaction mechanisms, facilitated by the presence of free electrons on the $-NH_2$ and $-OH$ surface groups of CS, which interact with metal ions by filling empty d-orbitals to form complexes.[23] Meanwhile, the role and effectiveness of CS when modified with some materials in the treatment of arsenic have also been mentioned in literature reports.[24]

In this study, the "waste to adsorbent" strategy was proposed, in which solid waste from heavy industrial processes is treated to produce nanostructured Fe_3O_4 materials for arsenic pollution remediation. This strategy serves two functions simultaneously: (1) the synthesis process of the Fe_3O_4 material does not generate additional hazardous waste; and (2) solid waste sources undergo cleaning processes and pollution reduction measures to mitigate environmental contamination. Moreover, the materials are also evaluated for their properties and arsenic isothermal adsorption process kinetics in an aqueous environment.

2. EXPERIMENTAL SECTION

2.1. Materials. Ferrous chloride tetrahydrate ($FeCl_2 \cdot 4H_2O$), ascorbic acid ($C_6H_8O_6$), sodium borohydride ($NaBH_4$), hydrochloric acid (HCl), potassium iodide (KI), sodium hydroxide (NaOH), and acetic acid (CH_3COOH) were purchased from Merck. Arsenic standard solution 1000 mg/L for AA (arsenic III-oxide in 0.5 M nitric acid solution, d = 1.01 g/cm^3) was purchased from Scharlau, Spain. Ammonium hydroxide (NH_4OH) was obtained from Macklin-China, India. The red mud was from Central Highlands, Vietnam (particle size ≤200 μm; main components include Al_2O_3:14.0%, CaO: 2.3%, Fe_2O_3: 55.5%, SiO_2: 5.3%, and MKN: 11.1%). All chemical solutions were diluted with distilled water until the desired concentration was reached.

2.2. Synthesis Methods. *2.2.1. Synthesis of Fe_3O_4/CS Nanocomposites.* The method of synthesizing Fe_3O_4 nanoparticles using the Central Highlands red mud followed a previous ultrasound-assisted coprecipitation method (Scheme 1).[19]

The red sludge was dissolved in deionized water with a weight ratio of 5 liquid:1 solid and stirred until the pH reached equilibrium in the range of 7.5−8.0 and then dried at 80 °C for 24 h. The sample received was about 50% iron oxide in weight, and it was further treated with H_2SO_4 2 M solution for 3 days at room temperature. Then a red solution was obtained after being filtered to remove the insoluble materials.

$FeCl_2 \cdot 4H_2O$ was added to a 100 mL brown-red solution (with a molar ratio of 2 Fe^{3+}:1 Fe^{2+}) with vigorous stirring under a N_2 gas flow for 10 min. The mixed solution was sonicated with a VCX500 probe sonicator operating at a frequency of 20 kHz. The reaction flask was then slowly filled with a 25−28% NH_3 solution in weight, ensuring that the solution always maintained a pH of 9−10. During this process, the solution's color changed from yellow-orange to brown before becoming black. Then, the solution was allowed to react with a sufficient amount of NH_3 for 30 min while maintaining the original conditions. Next, the Fe_3O_4 NPs were dried at 70 °C under vacuum for 12 h after being separated by a magnet and washed several times in ethanol and deionized water.

The method to prepare Fe_3O_4/CS nanocomposites was previously presented in a publication by Nguyen et al.[25] First, sonication was used to dissolve 0.5 g of CS in 50 mL of acetic acid to obtain a 1% CS/CH_3COOH solution. After that, 5 g of Fe_3O_4 NPs was added, and the mixed solution was sonicated

https://doi.org/10.1021/acsomega.4c05955
ACS Omega 2025, 10, 3351−3360

for 1 h. Finally, the Fe_3O_4/CS product was dried on Petri dishes in an oven at 60 °C for 24 h.

2.2.2. Study Material Properties. The structure phase and magnetic properties of the materials were characterized by X-ray diffraction (XRD) using Cu Kα (λ = 1.5406 Å) radiation and vibrating sample magnetometry (VSM). In addition, the FTIR technique was also used to determine the chemical bonds, composition, covalent bond pairs, and functional groups in the material.

The surface morphology of the materials was determined by FESEM measurement using a Hitachi S-4800. The sample preparation for FESEM measurement was as follows: a small amount of sample was dissolved in an ethanol solution, and a few drops of the mixture were placed on an aluminum grid. Then, it was allowed to dry for 1−2 h in a vacuum at over 40 °C. The solid samples were subjected to magnetic measurements at room temperature (25 °C) utilizing a Magnet B-10 vibrating sample magnetometer.[19]

Experimental studies of static desorption and adsorbed were conducted at 77 K to determine the specific surface areas and pore size distributions. The preparation has been described in a previous study.[19]

2.2.3. Batch Adsorption Procedure. Adsorption ability was determined by the batch method so that we could find the main factors influencing adsorption. They were the adsorbent dose, temperature, initial arsenic(III) concentration, and time. Hence, optimization was calculated to achieve maximum process efficiency.

In this study, a predetermined amount of nanocomposites was added continuously to the As(III) solution flask and shaken until the pH value reached equilibrium at a temperature of 303 ± 1 K. Subsequently, the flask was continually shaken at 240 rpm before the inside solution was filtered through a magnet and stored in polythene tubes. The solution was then diluted for further analysis. The experimental conditions of this procedure are the same as previously reported,[19] including adsorbent dosage (0.25−2.5 g/L), pH (2.0−10.0), the initial As(III) concentration (5.0−25.0 mg/L), temperature (293−313 K), and time (0−180 min). Besides, the pH value was adjusted by 0.1 N HCl or 0.1 N NaOH solutions.

For the adsorption isotherm study, 0.5 g/L doses of Fe_3O_4/CS nanocomposite were added to flasks having 100 mL As(III) solutions (5−25 mg/L at concentration) at a predetermined temperature and pH. The optimum adsorption time was 1 h. All of the experiments were triplicated, and their standard deviation was 2.0%.

The experiments for thermodynamic studies were repeated at 297−903 and 313 K. Kinetic studies were also carried out at various initial arsenic concentrations ranging from 5 to 25 mg/L at 303 K, at equal time intervals.

2.2.4. Analysis of As(III) Ion Concentration. The adsorbent concentration was measured using an atomic fluorescence spectrophotometer (AFS), AFS 240-Agilent, modular VGA 77 vapor, and using the hydride technique.

The adsorption capacity (q) was calculated by the formula[26]

$$q = \frac{(C_o - C_t)\cdot V}{m} \quad (1)$$

where q, C_o, C_t, V, and m are As(III) uptake capacity (mg/g), initial As(III) concentration (mg/L), As(III) concentration at time t (mg/L), the volume of the treated solution (L), and adsorbent weight (g), respectively.

The removal efficiency (%R) of As(III) was calculated as follows:

$$\%R = \frac{C_0 - C_e}{C_0} \times 100 \quad (2)$$

Here, C_e is the As(III) concentration at equilibrium (mg/L).

3. RESULTS AND DISCUSSION

3.1. Characterization of the Fe_3O_4/CS Nanocomposites. The XRD data of the Fe_3O_4/CS nanocomposite is demonstrated in Figure 1. The characteristic peaks at 30.42°, 35.97, 43.38, 57.3, and 63.05° correspond to (220), (311), (222), (511), and (440), respectively. These peaks belong to a phase of Fe_3O_4 nanoparticles (ICSD 01−071−6339) (Figure S1). CS demonstrates two distinct crystalline peaks, located at approximately 20 and 10.8°. The presence of numerous hydroxyl and amino groups within the CS structure initiates the creation of hydrogen bonds, thereby facilitating the

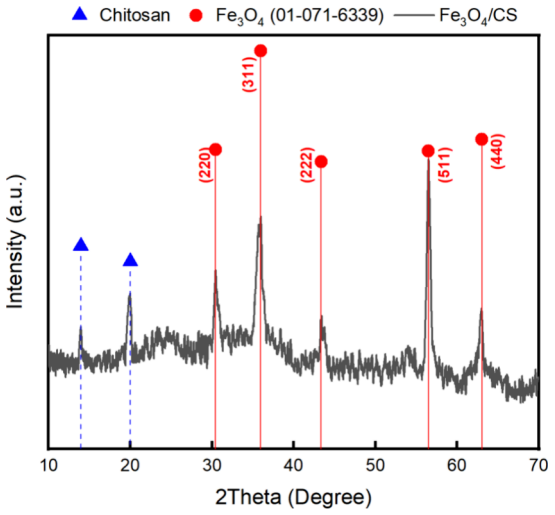

Figure 1. XRD profile of Fe_3O_4/CS.

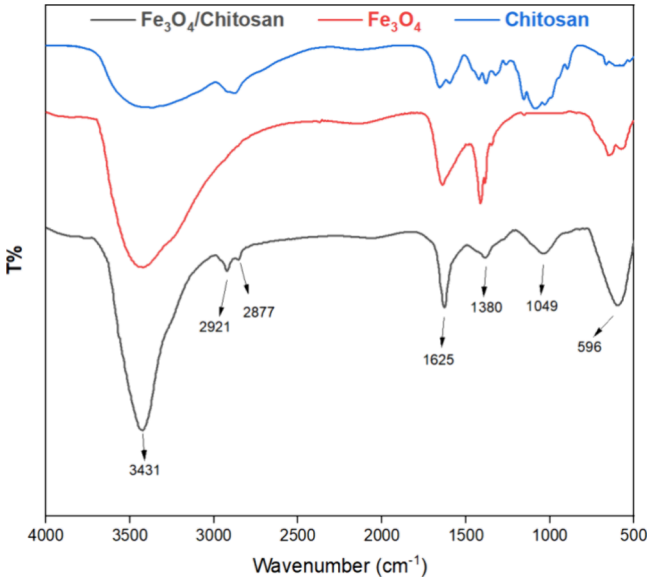

Figure 2. FTIR spectra of Fe_3O_4, CS, and Fe_3O_4/CS.

https://doi.org/10.1021/acsomega.4c05955
ACS Omega 2025, 10, 3351−3360

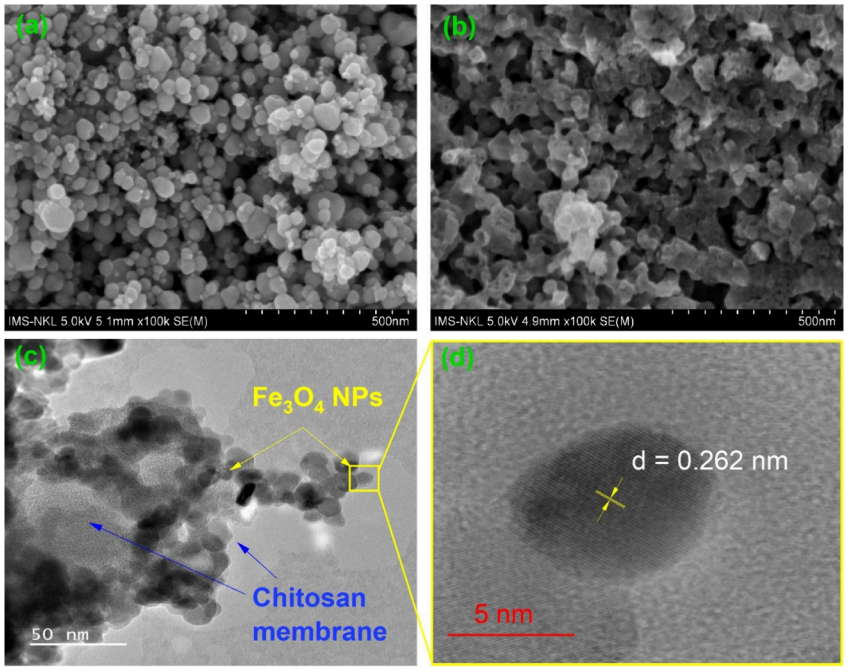

Figure 3. FESEM images of Fe_3O_4 NPs (a), Fe_3O_4/CS (b), and TEM images of Fe_3O_4 with the scale of 50 nm (c) and 10 nm (d).

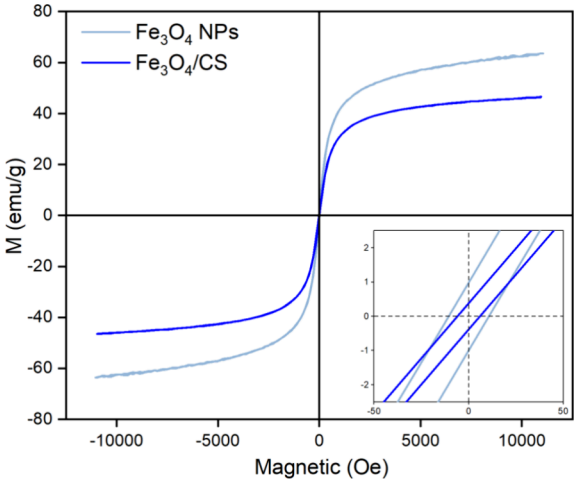

Figure 4. Magnetic hysteresis curves (M-H) of Fe_3O_4 NPs and Fe_3O_4/CS.

establishment of a uniform crystalline structure within the CS molecules, as observed in prior research.[27]

Figure 2 presents the FTIR spectra of bare Fe_3O_4, CS, and Fe_3O_4/CS nanoparticles. The peak observed around 3431 cm^{-1} in both Fe_3O_4 and Fe_3O_4/CS samples is associated with the −OH stretching vibration.[28] For the Fe_3O_4 nanoparticles, the peaks located at approximately 579 and 650 cm^{-1} are attributed to the Fe−O stretching vibration.[29] In the FTIR spectrum of CS, the absorption bands around 2921 and 2877 cm^{-1} correspond to the symmetric and asymmetric stretching of C−H bonds, respectively, while the broad peak around 1049 cm^{-1} is due to the C−O stretching, and the peak at 1625 cm^{-1} is related to the C═O stretching of amide I.[30] In the spectrum of Fe_3O_4/CS nanoparticles, all characteristic peaks of CS and Fe_3O_4 nanoparticles are almost present. However, some minor deviations in peak positions and the merging of peaks into broader peaks are observed. This observation may be due to the overlap of vibrations, for example, the broad peak at position 598 cm^{-1} of the Fe_3O_4/CS may be due to the overlap of −OH group vibrations of CS[31] and the Fe−O vibration of Fe_3O_4. The results pointed out that CS was coated on Fe_3O_4 nanoparticles successfully.

The morphologies of Fe_3O_4 NPs and Fe_3O_4/CS are displayed in Figure 3a,b, respectively. It is clear that the distribution of Fe_3O_4 NPs is uniform (from 10 to 30 nm) and that CS is present on the surface of these particles. This result was also confirmed through TEM images (Figure 3c). Furthermore, the magnified TEM image presented in Figure 3d revealed lattice fringes with an interlayer spacing of 0.262 nm, which closely corresponds to the *d*-spacing of the (311) plane in cubic Fe_3O_4.[32]

Figure 4 shows the magnetic properties of Fe_3O_4 NPs and Fe_3O_4/CS nanocomposite samples by VSM spectra. The results of saturation magnetization of Fe_3O_4 NPs and Fe_3O_4/CS nanocomposites are 63.2 and 50.2 emu/g, which indicate that both synthesized materials were superparamagnetic. The reduction in magnetization is likely attributed to the presence of the antiferromagnetic organic coating, specifically the CS layer, as confirmed by morphology and structure analysis. For this reason, the material can be easily separated from the aqueous solution in the presence of an external magnetic field, especially after the adsorption process.[33] In addition, the graph also reveals that the coated nanoparticles exhibit superior superparamagnetic properties, characterized by a lower remnant magnetization (M_r = 0.38 emu/g) and coercivity (C_e = 5.9 Oe).

The hydrodynamic diameter of the nanocomposites in dilute aqueous suspensions is determined by DLS (Figure 5a). The size-distribution curve of Fe_3O_4/CS has only one peak at a size of around 165 nm, larger than the average size of Fe_3O_4 particles. The zeta potential of Fe_3O_4/CS is 25.02 mV (Figure 5b), which is also much larger than that of the Fe_3O_4 NPs (6.9 mV). This enhancement may be due to the protonation of free amine groups on the surface of CS.[34] Additionally, the Brunauer−Emmett−Teller theory data indicates that the

https://doi.org/10.1021/acsomega.4c05955
ACS Omega 2025, 10, 3351−3360

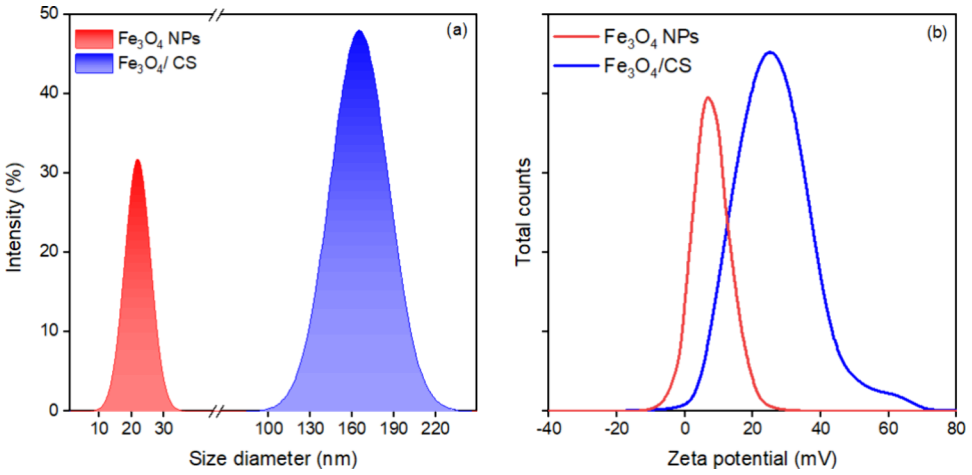

Figure 5. (a) Size distribution and (b) zeta potential of Fe_3O_4 NPs and Fe_3O_4/CS.

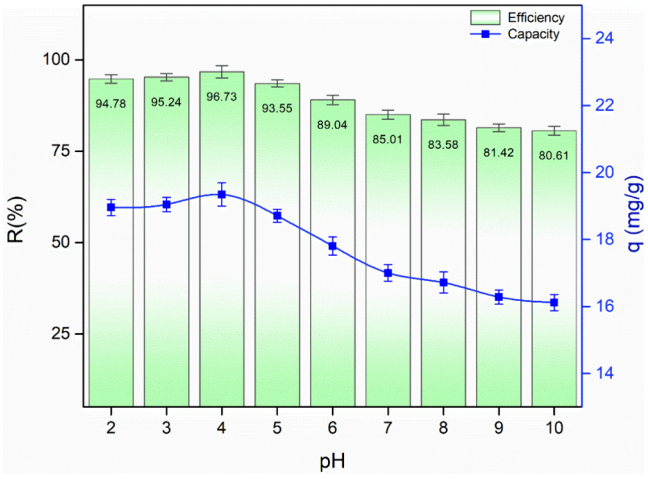

Figure 6. Effect of pH (adsorbent dosage = 0.5 g/L; [As(III)] = 10 mg/L; t = 90 min).

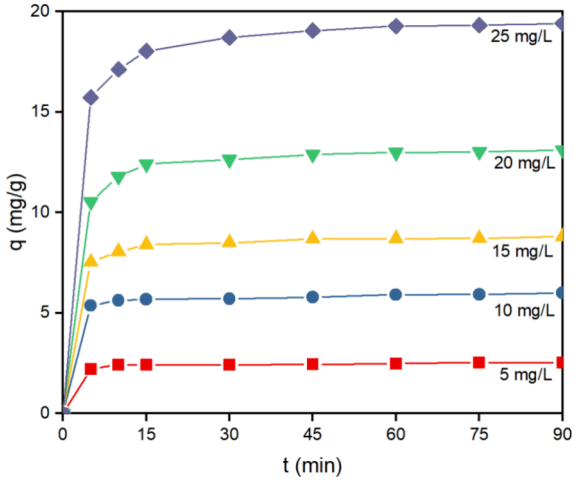

Figure 7. Effect of time on adsorption capacity (adsorbent dosage = 0.5 g/L; pH = 4.0; agitation: 240 rpm).

specific surface area of the material system increased to 93.64 m^2/g after the addition of CS, which is higher than that of Fe_3O_4 NPs at 88.94 m^2/g (Figures S2 and S3). This also contributes to the enhanced adsorption performance of the material system as the active surface increases.

3.2. Adsorption Studies. *3.2.1. Effect of pH on Arsenic Removal.* One of the most significant factors in As(III) removal is the pH. It can directly affect the removal efficiency of pollutants or the adsorbate because $[H^+]$ ions and $[OH^-]$ ions can interact with the activated site of adsorbents.[35]

In this experiment, the initial dose of As(III) was 10 mg/L; the initial pH values were adjusted in the range of 2−10, and the contact time was 3 h. Hence, the amount of adsorbate was controlled by pH adjustment. Figure 6 shows the effect of pH on the adsorption experiment at 303 K.

Generally, the efficiency decreased gradually when the pH increased. The optimal adsorption efficiency in acidic aqueous solutions at equilibrium was in the pH range of 2.0−4.0. The highest and lowest percentage removal efficiencies were 96.73% (at pH = 4) and 80.61% (at pH = 10). Guo and Chen[36] reported that As(III) is stable as H_3AsO_3 at pH < 9, while its other corresponding forms are $H_2AsO_3^-$ at pH = 9−12; $HAsO_3^{2-}$ at pH = 12−13; or AsO_3^{3-} at pH > 13. When the pH increased, the removal efficiency decreased due to the decrease in electrostatic attraction. The higher the pH, the higher the amount of negatively charged hydroxyl ions in solutions. As a result, these ions caused the impediment for the attraction between AsO_3^{3-} ions and Fe^{3+} ions.

3.2.2. Effect of Contact Time on Adsorption. Figure 7 represents the data of adsorption capacity (q) after 90 min at 5, 10, 15, 20, and 25 mg/L initial As(III) concentration at pH 4.0 and temperature 303 K.

The graph revealed that the adsorption capacity increased rapidly after 10 min at the beginning and moved sideways until adsorption equilibrium was reached at 90 min.

3.2.3. Adsorption Isotherm Study. The Langmuir, Freundlich, and Temkin isotherm models were calculated to explain the theoretical adsorption capacity of the nanocomposite. They can be denoted as eq 3−5, respectively.[37]

$$\frac{1}{q_e} = \left(\frac{1}{q_{max} \cdot K_L}\right) \times \frac{1}{C_e} + \frac{1}{q_{max}} \tag{3}$$

$$\log q_e = \log K_F + \frac{1}{n} \log C_e \tag{4}$$

$$Q_e = \frac{R \cdot T}{b_T} \ln A_T + \frac{R \cdot T}{b_T} \ln C_e \tag{5}$$

https://doi.org/10.1021/acsomega.4c05955
ACS Omega 2025, 10, 3351−3360

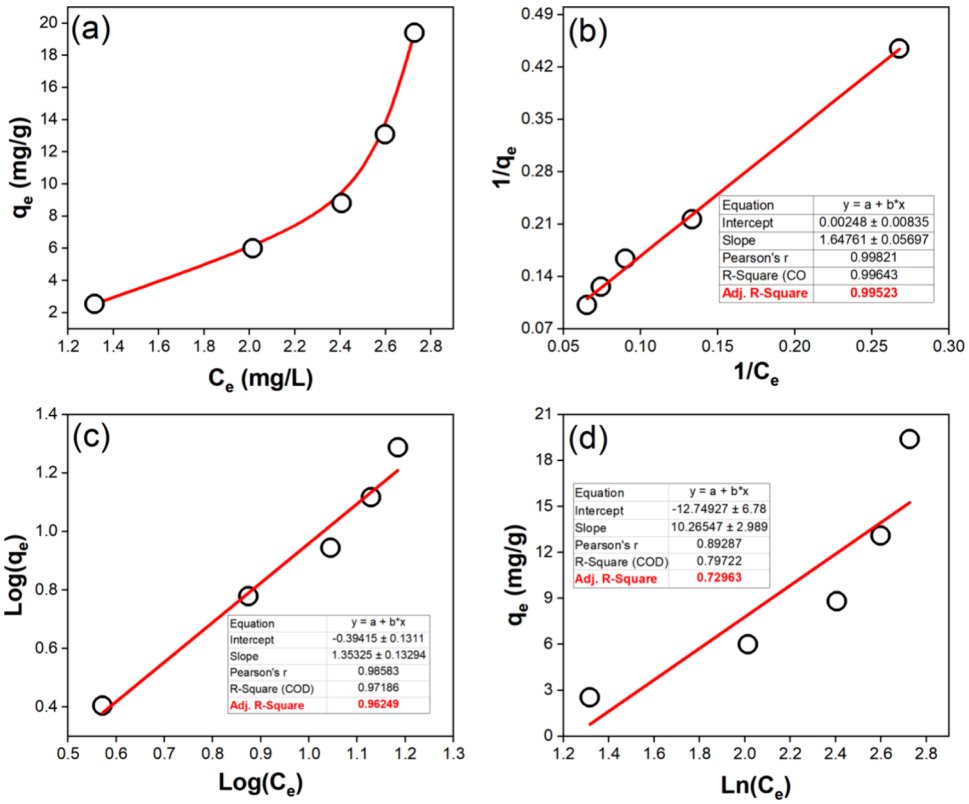

Figure 8. Isotherm curve (a) and the fitting plots of Langmuir (b), Fruendlich (c), and Temkin (d) adsorption isotherm models.

Table 1. Langmuir, Freundlich, and Temkin Isotherm Constants

model	parameters	
Langmuir	Intercept	0.002
	Slope	1.647
	R^2	0.995
	K_L (L/mg)	0.028
	q_{max} (mg/g)	21.04
	R_L	0.776
Freundlich	Intercept	−0.394
	Slope	1.353
	R^2	0.962
	K_F	2.477
	N	0.738
Temkin	Intercept	2.160
	Slope	0.083
	R^2	0.729
	a_T (L/mg)	0.288
	b_T (J/mol)	10.265

Here, C_e is the equilibrium concentration of As (III) (mg/L), q_{max} is the maximum uptake capacity (mg/g), K_L is the Langmuir constant (L/mg), K_F is the Freundlich constant, n is the constant integrating intensity, b_T represents the Temkin constant associated with the heat of adsorption (J/mol), a_T is the Temkin isotherm equilibrium binding constant (L/mg), R is the gas constant valued at 8.3145 J/mol K, and T denotes the absolute temperature, which is 303 K.[38]

Figure 8 presents the isotherm curve (a) as well as the Langmuir (b), Freundlich (c), and Temkin (d) isotherm models analyzed through linear regression. The close fit and high linear determined coefficients ($R^2 > 0.99$) suggest that the adsorption behavior of the adsorbent adheres to the Langmuir model, indicating monolayer adsorption of heavy metals on the surface. Additionally, the fitting parameters derived from the Freundlich and Temkin models are included and exhibit significant deviations (Table 1).

3.2.4. Adsorption Kinetics Study. The pseudo-first-order model, pseudo-second-order model, intraparticle diffusion model, and Elovich model were utilized to study the adsorption kinetics of the nanocomposite. Their formulas are as follows, respectively.[39]

$$\ln(q_e - q_t) = \ln(q_e) - k_1 t \quad (6)$$

$$\frac{t}{q_t} = \frac{t}{q_e} + \frac{1}{k_2 . q_e^2} \quad (7)$$

$$\ln(q_t) = \ln(k_D) + 0.5 . \ln(t) \quad (8)$$

$$q_t = \frac{1}{\beta}\ln(\alpha\beta) + \frac{1}{\beta}\ln(t) \quad (9)$$

Here, k_1 (min^{-1}) is a pseudo-first-order kinetic constant, k_2 (mg/g.min) is a pseudo-second-order kinetic constant, k_D (mg/g $(min)^{1/2}$) is the diffusion coefficient, and α and β are constants of the Elovich equation.

There are plots of $\ln(q_e - q_t)$ versus t value (pseudo-first-order), t/q_t value versus t value (pseudo-second-order), $\ln(q_t)$ versus $\ln(t)$ (intraparticle model), and q_t versus $\ln(t)$ (Elovich model) as represented in Figure 9.

According to Table 2, the linear fitting lines and the R^2 values of the pseudo-second-order model were relatively high ($R^2 > 0.99$). This indicated that chemical adsorption served as the rate-limiting step, involving valence forces through electron exchange between the adsorbate and the adsorbent phases.[40]

https://doi.org/10.1021/acsomega.4c05955
ACS Omega 2025, 10, 3351−3360

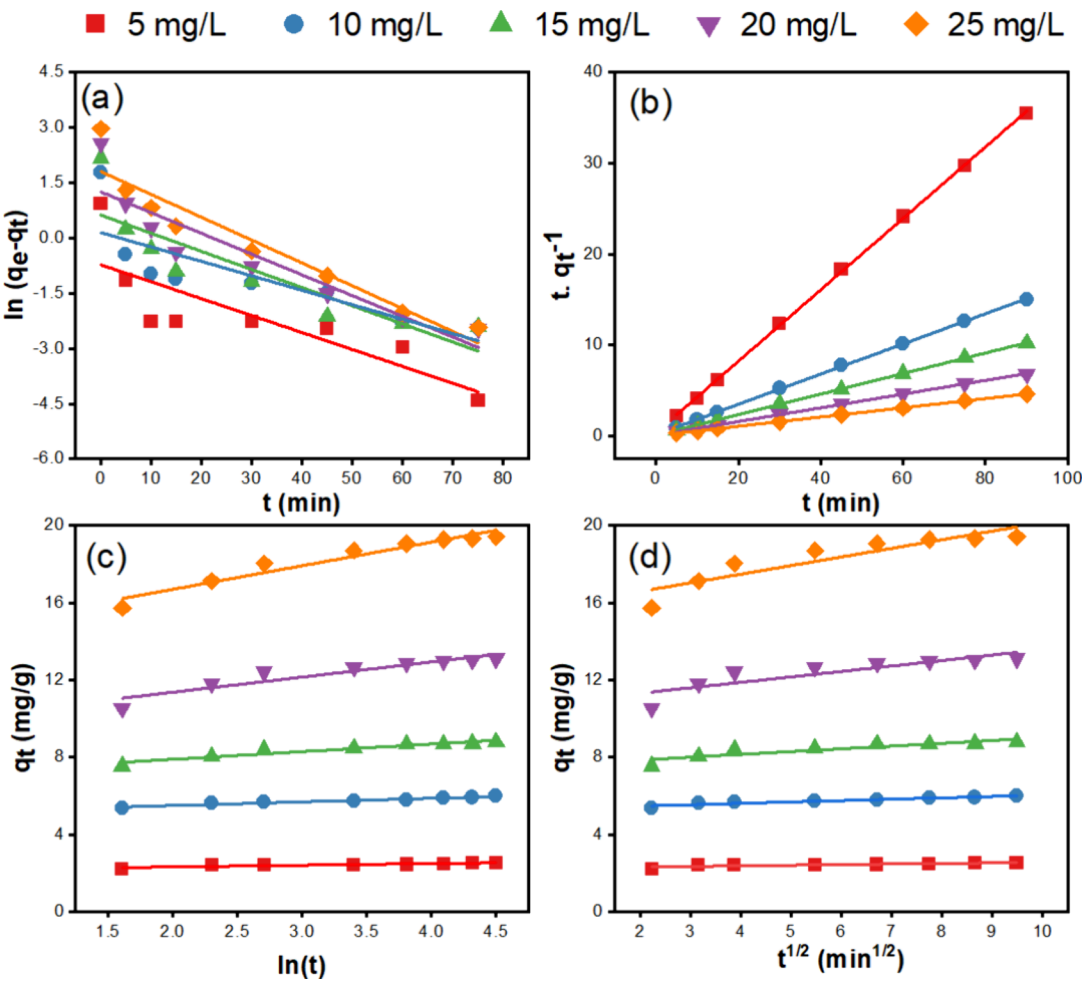

Figure 9. Kinetic-model plots of As (III) adsorption. (a) Pseudo-first-order model, (b) pseudo-second-order model, (c) intraparticle diffusion model, and (d) Elovich model.

Table 2. Pseudo-First-Order Model, Pseudo-Second-Order Model, intraparticle Diffusion Model, and Elovich Kinetic-Model Parameters

			parameters				
model	linear equation	conc. (mg/L)	5	10	15	20	25
Pseudo First Order	$\ln(q_e - q_t) = \ln(q_e) - k_1 t$	Intercept	−0.726	0.150	0.625	1.255	1.806
		Slope	−0.046	−0.039	−0.049	−0.056	−0.062
		R^2	0.632	0.614	0.719	0.826	0.891
		k_1 (min^{-1})	-6.1×10^{-4}	-5.2×10^{-4}	-6.5×10^{-4}	-7.4×10^{-4}	-8.2×10^{-4}
		q_e, cal (mg/g)	0.484	1.162	1.868	3.508	6.086
Pseudo Second Order	$\frac{t}{q_t} = \frac{1}{k_2 q_e^2} + \frac{t}{q_e}$	Intercept	0.374	0.176	0.113	0.095	0.072
		Slope	0.392	0.166	0.112	0.075	0.050
		R^2	**0.999**	**0.999**	**0.999**	**0.999**	**0.999**
		k_2 (g/mg min)	0.411	0.157	0.111	0.059	0.035
		q_e, cal (mg/g)	2.551	6.024	8.929	13.333	20.000
Elovich	$q_t = \frac{1}{\alpha}\ln(\alpha\beta) + \frac{1}{\alpha}\ln t$	Intercept	2.160	5.122	7.103	9.786	14.244
		Slope	0.083	0.187	0.394	0.786	1.220
		R^2	0.766	0.9367	0.909	0.874	0.938
		α (mg/g min)	12.048	5.319	2.538	1.272	0.819
		β (g/mg)	1.66×10^{10}	1.28×10^{11}	2.66×10^{7}	2.01×10^{5}	1.43×10^{5}
intraparticle diffusion	$q_t = K_{diff} t^{1/2} + C$	Intercept	2.258	5.324	7.572	10.74	15.683
		Slope	0.030	0.072	0.143	0.282	0.446
		R^2	0.680	0.906	0.791	0.742	0.825
		K_{diff}	0.030	0.072	0.143	0.282	0.446
		C	2.258	5.324	7.572	10.74	15.683

https://doi.org/10.1021/acsomega.4c05955
ACS Omega 2025, 10, 3351−3360

Table 3. Thermodynamic Parameters for As (III) Adsorption at Different Temperatures

temperature (K)	ΔG° (kJ/mol)	ΔS° (J/mol K)	ΔH° (kJ/mol)
293	−0.579		
303	−1.355	81.227	23.258
313	−2.223		

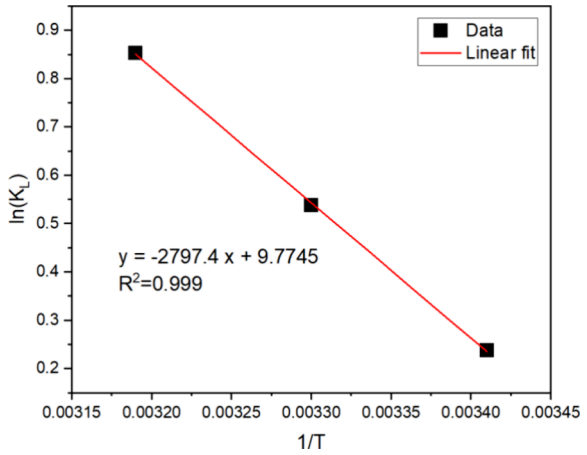

Figure 10. Plot of the thermodynamic model (adsorbent dosage 0.5 g/L; pH 4.0; t = 120 min; agitation 240 rpm).

Meanwhile, the equations of the other models at each concentration had unsuitable correlation coefficients, indicating that the adsorption process did not follow the results of these models, which is consistent with a previous study.[41] The experimental q_e values (determined from Figure 7) also corresponded more accurately with the q_e values derived from the pseudo-second-order kinetic model. Thus, this model proved to be more effective in validating the adsorption process, compared to other models.

3.2.5. Thermodynamic Study. The thermodynamics of As(III) onto the Fe_3O_4/CS nanocomposite was studied by the following equations:[42]

$$\Delta G^\circ = -RT\ln(K_L) \quad (10)$$

$$\ln(K_L) = \frac{\Delta S^\circ}{R} - \frac{\Delta H^\circ}{R \cdot T} \quad (11)$$

Here, R, ΔH°, ΔG°, ΔS°, and K_L correspond to the universal gas constant (8.314 J/mol K), the enthalpy change (kJ/mol), the free energy change (J/mol), the entropy change (kJ/mol K), and the Langmuir isotherm constant, respectively. Using the straight-line plots of $\ln(K_L)$ versus $1/T$, the ΔS° and ΔH° values could be determined by the intercept and slope of the drawn lines. The parameters and thermodynamic data are given next (Table 3 and Figure 10, respectively).

As shown in Table 3, the positive change in enthalpy (ΔH° = 23.258) signifies that the adsorption process is an endothermic process, whereas the positive change in entropy (ΔS° = 81.227) indicates an increase in randomness at the solid/solution interface.[43] Gibbs free energy ΔG° values were −0.579, −1.355, and −2.223 at temperatures of 293, 303, and 313 K, respectively. Hence, the adsorption process is spontaneous in nature and is better at lower temperatures.[44]

In Table 4, the maximum adsorption capacity (Q_{max}) and As removal efficiency (H) of the Fe_3O_4/CS nanocomposite synthesized in this study are compared with those of similar Fe_3O_4-based materials from previous studies. The results indicate that Fe_3O_4/CS exhibits good performance and holds potential for the treatment of As(III) in contaminated water sources.

4. CONCLUSIONS

The Fe_3O_4/CS nanocomposite was synthesized using red mud (Central Highlands, Vietnam) by the ultrasonic-assisted coprecipitation method with a relative size of 165 nm. The results of XRD, FESEM, and TEM proved that the nanocomposite material was successfully synthesized. The batch uptake experimental results indicated that the nanocomposite is a promising adsorbent for As(III) removal application. The adsorption equilibrium data is suitable for Langmuir isotherm models. The adsorption process is a physical and exothermic process, as proven by the pseudo-second-order kinetic model and thermodynamic study.

■ ASSOCIATED CONTENT

Supporting Information

The Supporting Information is available free of charge at https://pubs.acs.org/doi/10.1021/acsomega.4c05955.

XRD data of synthesized Fe_3O_4 NPs (Figure S1) and nitrogen adsorption/desorption isotherm plots of Fe_3O_4/CS and Fe_3O_4 NPs (Figures S2 and S3) (PDF)

Table 4. Comparison of the Removal Efficiency with Those in Literature Reports

materials	Q_{max} − H (mg/g)-(%)	arsenic (conc.)	year (ref)
BNNS-Fe_3O_4 (Fe_3O_4-functionalized boron nitride nanosheets)	24.5 mg/g (0.4 g/L)	As (III) in water (As(III) ions from 134 to 2.67 ppb, 25 °C)	2020[2]
BMN (Biomass-derived magnetic nanocomposite)	16.23 mg/g (2.0 g/L)	As (III) in water (As(III) ions 50 ppm, 25 °C)	2020[45]
MTHCNPs (Magnetic composite microparticles based on Fe_3O_4, TiO_2, and CS)	33.68 mg/g (6.7 g/L)	As (III) in water (As(III) ions 5.0 ppm, 40 °C)	2023[46]
	34.61 mg/g (6.7 g/L)	As (V) in water (As(V) ions 5.0 ppm, 40 °C)	
Fe_3O_4/CS/PEI Modification of magnetic CS (Fe_3O_4/CS) with polyethylenimine (PEI)	77.61 mg/g − 99.5% (0.5 g/L)	As (III) in water (As(III) ions 2.0 ppm, 30 °C)	2021[47]
	86.50 mg/g − 99.7% (0.5 g/L)	As (V) in water (As(V) ions 1.5 ppm, 30 °C)	
Fe_2O_3 Activated hematite iron ore/Balochistan, Pakistan	14.46 mg/g − 95.0% (15.0 g/L)	As (III) in water (As(III) ions 150 ppm, 25 °C)	2020[48]
Fe_3O_4/CS Magnetic CS nanocomposites derived from industrial solid waste	21.04 mg/g − 96.73% (0.5 g/L)	As (III) in water (As(III) ions 100 ppm, 303 K)	This work

https://doi.org/10.1021/acsomega.4c05955
ACS Omega 2025, 10, 3351−3360

AUTHOR INFORMATION

Corresponding Author

Nguyen Thi Huong − *Institute of Chemistry and Materials, Ha Noi 100000, Vietnam;* orcid.org/0000-0003-2716-936X; Email: nguyenhuong0916@gmail.com

Authors

Le Minh Tri − *Academy of Military Science and Technology, Hanoi 100000, Vietnam*

Pham Thi Mai Huong − *Hanoi University of Industry, Ha Noi 100000, Vietnam*

Complete contact information is available at: https://pubs.acs.org/10.1021/acsomega.4c05955

Notes

The authors declare no competing financial interest.

ACKNOWLEDGMENTS

The authors thank the Institute of Chemistry and Materials for the support of this work.

REFERENCES

(1) Soliman, N. K.; Moustafa, A. Industrial solid waste for heavy metals adsorption features and challenges; a review. *Journal of Materials Research and Technology* **2020**, *9* (5), 10235−10253.

(2) Bangari, R. S.; Yadav, V. K.; Singh, J. K.; Sinha, N. Fe_3O_4-Functionalized boron nitride nanosheets as novel adsorbents for removal of arsenic (III) from contaminated water. *ACS omega* **2020**, *5* (18), 10301−10314.

(3) Pathan, S.; Bose, S. Arsenic removal using "green" renewable feedstock-based hydrogels: current and future perspectives. *ACS omega* **2018**, *3* (5), 5910−5917.

(4) Zandsalimi, S.; Karimi, N.; Kohandel, A. Arsenic in soil, vegetation and water of a contaminated region. *International Journal of Environmental Science & Technology* **2011**, *8*, 331−338.

(5) Liu, F.; Yang, W.; Li, W.; Zhao, G.-C. Simultaneous oxidation and sequestration of arsenic (III) from aqueous solution by copper aluminate with peroxymonosulfate: A fast and efficient heterogeneous process. *ACS omega* **2021**, *6* (2), 1477−1487.

(6) Pu, G.; Zeng, D.; Mo, L.; Liao, J.; Chen, X.; Qiu, S.; Lv, Y. Artificial light at night alter the impact of arsenic on microbial decomposers and leaf litter decomposition in streams. *Ecotoxicology and Environmental Safety* **2020**, *191*, No. 110014.

(7) Abejón, A.; Garea, A.; Irabien, A. Arsenic removal from drinking water by reverse osmosis: Minimization of costs and energy consumption. *Sep. Purif. Technol.* **2015**, *144*, 46−53.

(8) Kundu, S.; Naskar, M. K. Perspective of membrane processes for the removal of arsenic from water: an overview. *Transactions of the Indian Ceramic Society* **2021**, *80* (1), 28−40.

(9) Oehmen, A.; Valerio, R.; Llanos, J.; Fradinho, J.; Serra, S.; Reis, M. A.; Crespo, J. G.; Velizarov, S. Arsenic removal from drinking water through a hybrid ion exchange membrane−coagulation process. *Sep. Purif. Technol.* **2011**, *83*, 137−143.

(10) (a) Fernando, M. S.; Wimalasiri, A.; Dziemidowicz, K.; Williams, G. R.; Koswattage, K.; Dissanayake, D.; de Silva, K. N.; de Silva, R. M. Biopolymer-based nanohydroxyapatite composites for the removal of fluoride, lead, cadmium, and arsenic from water. *ACS omega* **2021**, *6* (12), 8517−8530. (b) Singh, P.; Sarswat, A.; Pittman, C. U., Jr; Mlsna, T.; Mohan, D. Sustainable low-concentration arsenite [As (III)] removal in single and multicomponent systems using hybrid iron oxide−biochar nanocomposite adsorbents—A mechanistic study. *Acs Omega* **2020**, *5* (6), 2575−2593.

(11) Wang, C.; Luan, J.; Wu, C. Metal-organic frameworks for aquatic arsenic removal. *Water research* **2019**, *158*, 370−382.

(12) Ahmad, K.; Shah, H.-U.-R.; Nasim, H. A.; Ayub, A.; Ashfaq, M.; Rauf, A.; Shah, S. S. A.; Ahmad, M. M.; Nawaz, H.; Hussain, E. Synthesis and characterization of water stable polymeric metallo organic composite (PMOC) for the removal of arsenic and lead from brackish water. *Toxin Reviews* **2022**, *41* (2), 577−587.

(13) Lee, S. M.; Tiwari, D. Porous hybrid materials in the remediation of water contaminated with As(III) and As(V). *Chem. Eng. J.* **2015**, *270*, 496−507.

(14) Gupta, A. D.; Rene, E. R.; Giri, B. S.; Pandey, A.; Singh, H. Adsorptive and photocatalytic properties of metal oxides towards arsenic remediation from water: A review. *Journal of Environmental Chemical Engineering* **2021**, *9* (6), No. 106376.

(15) Siddiqui, S. I.; Chaudhry, S. A. Iron oxide and its modified forms as an adsorbent for arsenic removal: A comprehensive recent advancement. *Process Safety and Environmental Protection* **2017**, *111*, 592−626.

(16) (a) Ge, S.; Shi, X.; Sun, K.; Li, C.; Uher, C.; Baker, J. R., Jr; Banaszak Holl, M. M.; Orr, B. G. Facile hydrothermal synthesis of iron oxide nanoparticles with tunable magnetic properties. *J. Phys. Chem. C* **2009**, *113* (31), 13593−13599. (b) Li, S.; Zhang, T.; Tang, R.; Qiu, H.; Wang, C.; Zhou, Z. Solvothermal synthesis and characterization of monodisperse superparamagnetic iron oxide nanoparticles. *J. Magn. Magn. Mater.* **2015**, *379*, 226−231.

(17) Huong, T. M. P.; Con, H. T.; Dung, T. T. Study on the adsorption of Arsenate in Aqueous solution by Tay Nguyen Red Mud after separating the Aluminium and other soluble components in Alkaline solution. *VNU J. Sci.: Earth Environ. Sci.* **2017**, 331.

(18) Linh, H. X.; Thuan, H. D.; Phuong, D. T. H.; Thuy, N. T.; Hai, N. T.; Huy, N. N.; Van Thanh, D. Preparation of red mud/graphene composite and its application for adsorption of As (III) from aqueous solution. *Vietnam J. Sci. Technol.* **2017**, *55* (4C), 217−223.

(19) Thi Huong, N.; Son, N. N.; Phuong, V. H.; Dung, C. T.; Huong, P. T. M.; Son, L. T. Synthesis Fe_3O_4/Talc nanocomposite by coprecipition-ultrasonication method and advances in hexavalent chromium removal from aqueous solution. *Adsorption Science & Technology* **2020**, *38* (9−10), 483−501.

(20) Minh, N. C.; Van Hoa, N.; Trung, T. S. Preparation, properties, and application of low-molecular-weight chitosan. In *Handbook of Chitin and Chitosan*; Elsevier, 2020; 453−471.

(21) Feng, G.; Ma, J.; Zhang, X.; Zhang, Q.; Xiao, Y.; Ma, Q.; Wang, S. Magnetic natural composite Fe_3O_4-chitosan@ bentonite for removal of heavy metals from acid mine drainage. *J. Colloid Interface Sci.* **2019**, *538*, 132−141.

(22) Ge, J.; Zhai, M.; Zhang, Y.; Bian, J.; Wu, J. Biocompatible Fe_3O_4/chitosan scaffolds with high magnetism. *Int. J. Biol. Macromol.* **2019**, *128*, 406−413.

(23) Desbrières, J.; Guibal, E. Chitosan for wastewater treatment. *Polym. Int.* **2018**, *67* (1), 7−14.

(24) (a) Ayub, A.; Raza, Z. A. Arsenic removal approaches: A focus on chitosan biosorption to conserve the water sources. *Int. J. Biol. Macromol.* **2021**, *192*, 1196−1216. (b) Kwok, K. C. M.; Koong, L. F.; Al Ansari, T.; McKay, G. Adsorption/desorption of arsenite and arsenate on chitosan and nanochitosan. *Environmental Science and Pollution Research* **2018**, *25* (15), 14734−14742.

(25) Nguyen Thi, H.; Mai, P. T.; Viêm Đu'c, Đ.; Nguyen Ngoc, S.; Lê Duc, A.; Nguyen Viet, H.; Vũ Minh, T. Ultrasound assisted synthesis of Fe_3O_4/Chitosan nanocomposites from Tay Nguyen red mud and kinetic study of Cr(VI) in aqueous solution. *J. Mil. Sci. Technol.* **2022**, No. VITTEP, 62−71.

(26) Reczek, L.; Michel, M. M.; Trach, Y.; Siwiec, T.; Tytkowska-Owerko, M. The Kinetics of Manganese Sorption on Ukrainian Tuff and Basalt—Order and Diffusion Models Analysis. *Minerals* **2020**, *10*, 1065.

(27) Kausar, A.; Naeem, K.; Hussain, T.; Nazli, Z.-I.-H.; Bhatti, H. N.; Jubeen, F.; Nazir, A.; Iqbal, M. Preparation and characterization of chitosan/clay composite for direct Rose FRN dye removal from aqueous media: comparison of linear and non-linear regression methods. *Journal of Materials Research and Technology* **2019**, *8* (1), 1161−1174.

(28) Potlog, T.; Popusoi, A.; Lungu, I.; Robu, S.; Bulimestru, I. Photophysics of tetracarboxy-zinc phthalocyanine photosensitizers. *RSC Adv.* **2022**, *12* (49), 31778−31785.
(29) Mukhopadhyay, A.; Joshi, N.; Chattopadhyay, K.; De, G. A Facile Synthesis of PEG-Coated Magnetite (Fe_3O_4) Nanoparticles and Their Prevention of the Reduction of Cytochrome C. *ACS Appl. Mater. Interfaces* **2012**, *4* (1), 142−149.
(30) Fernandes Queiroz, M.; Melo, K. R.; Sabry, D. A.; Sassaki, G. L.; Rocha, H. A. Does the Use of Chitosan Contribute to Oxalate Kidney Stone Formation? *In Marine Drugs* **2015**, *13*, 141−158.
(31) Azlan, K.; Wan Saime, W. N.; Lai Ken, L. Chitosan and chemically modified chitosan beads for acid dyes sorption. *Journal of Environmental Sciences* **2009**, *21* (3), 296−302.
(32) Xiang, H.; Ren, G.; Zhong, Y.; Yang, X.; Xu, D.; Zhang, Z.; Wang, X. Characterization and synthesis of Fe_3O_4@C nanoparticles by in-situ solid-phase method. *Materials Research Express* **2021**, *8* (2), No. 025016.
(33) Lv, X.; Xue, X.; Jiang, G.; Wu, D.; Sheng, T.; Zhou, H.; Xu, X. Nanoscale zero-valent iron (nZVI) assembled on magnetic Fe3O4/graphene for chromium (VI) removal from aqueous solution. *J. Colloid Interface Sci.* **2014**, *417*, 51−59.
(34) Appu, M.; Lian, Z.; Zhao, D.; Huang, J. Biosynthesis of chitosan-coated iron oxide (Fe_3O_4) hybrid nanocomposites from leaf extracts of Brassica oleracea L. and study on their antibacterial potentials. *3 Biotech* **2021**, *11* (6), 271.
(35) Weber, W. J. *Adsorption processes.* **1974**, *37* (3), 375−392.
(36) Guo, X.; Chen, F. Removal of Arsenic by Bead Cellulose Loaded with Iron Oxyhydroxide from Groundwater. *Environ. Sci. Technol.* **2005**, *39* (17), 6808−6818.
(37) Ossman, M.; Mansour, M.; Fattah, M.; Taha, N.; Kiros, Y. Peanut shells and talc powder for removal of hexavalent chromium from aqueous solutions. *Bulg. Chem. Commun.* **2014**, *3* (3), 629−639.
(38) Araújo, C. S. T.; Almeida, I. L. S.; Rezende, H. C.; Marcionilio, S. M. L. O.; Léon, J. J. L.; de Matos, T. N. Elucidation of mechanism involved in adsorption of Pb(II) onto lobeira fruit (Solanum lycocarpum) using Langmuir. *Freundlich and Temkin isotherms. Microchemical Journal* **2018**, *137*, 348−354.
(39) (a) Sharma, M.; Chouksey, S.; Gond, L.; Bajpai, A. A hybrid bionanocomposite for Pb (II) ion removal from water: synthesis, characterization and adsorption kinetics studies. *Polym. Bull.* **2022**, *79* (12), 10675−10706. (b) Silva, L. M. S.; Muñoz-Peña, M. J.; Domínguez-Vargas, J. R.; González, T.; Cuerda-Correa, E. M. Kinetic and equilibrium adsorption parameters estimation based on a heterogeneous intraparticle diffusion model. *Surfaces and Interfaces* **2021**, *22*, No. 100791. (c) Simonin, J.-P. On the comparison of pseudo-first order and pseudo-second order rate laws in the modeling of adsorption kinetics. *Chemical Engineering Journal* **2016**, *300*, 254−263.
(40) Sen Gupta, S.; Bhattacharyya, K. G. Kinetics of adsorption of metal ions on inorganic materials: A review. *Adv. Colloid Interface Sci.* **2011**, *162* (1), 39−58.
(41) (a) Benettayeb, A.; Seihoub, F. Z.; Pal, P.; Ghosh, S.; Usman, M.; Chia, C. H.; Usman, M.; Sillanpää, M. Chitosan Nanoparticles as Potential Nano-Sorbent for Removal of Toxic Environmental Pollutants. *Nanomaterials* **2023**, *13* (3), 447. (b) Peng, X.; Mo, S.; Li, R.; Li, J.; Tian, C.; Liu, W.; Wang, Y. Effective removal of the rare earth element dysprosium from wastewater with polyurethane sponge-supported graphene oxide−titanium phosphate. *Environmental Chemistry Letters* **2021**, *19* (1), 719−728.
(42) Sulaiman, O.; Ghani, N. S.; Rafatullah, M.; Hashim, R. Removal of Zinc (II) Ions from Aqueous Solutions Using Surfactant Modified Bamboo Sawdust. *Sep. Sci. Technol.* **2011**, *46* (14), 2275−2282.
(43) Sahmoune, M. N. Evaluation of thermodynamic parameters for adsorption of heavy metals by green adsorbents. *Environmental Chemistry Letters* **2019**, *17* (2), 697−704.
(44) Sari, A.; Tuzen, M.; Citak, D.; Soylak, M. Equilibrium, kinetic and thermodynamic studies of adsorption of Pb(II) from aqueous solution onto Turkish kaolinite clay. *Journal of Hazardous Materials* **2007**, *149* (2), 283−291.
(45) Cui, J.; Jin, Q.; Li, Y.; Li, F. Oxidation and removal of As(iii) from soil using novel magnetic nanocomposite derived from biomass waste. *Environmental Science: Nano* **2019**, *6* (2), 478−488.
(46) Song, X.; Nong, L.; Zhang, Q.; Liu, J.; Zhang, S. Highly effective adsorption for both As(III) and As(V) in aqueous medium via magnetic chitosan-based composite microparticles: Low arsenic concentration, high column efficiency and adaptability. *Journal of Environmental Chemical Engineering* **2023**, *11* (5), No. 110874.
(47) Alsaiari, N. S.; Alzahrani, F. M.; Katubi, K. M.; Amari, A.; Rebah, F. B.; Tahoon, M. A. Polyethylenimine-Modified Magnetic Chitosan for the Uptake of Arsenic from Water. *Applied Sciences* **2021**, *11* (12), 5630.
(48) Memon, A. Q.; Ahmed, S.; Bhatti, Z. A.; Maitlo, G.; Shah, A. K.; Mazari, S. A.; Muhammad, A.; Jatoi, A. S.; Kandhro, G. A. Experimental investigations of arsenic adsorption from contaminated water using chemically activated hematite (Fe_2O_3) iron ore. *Environmental Science and Pollution Research* **2021**, *28* (10), 12898−12908.

https://doi.org/10.1021/acsomega.4c05955
ACS Omega 2025, 10, 3351−3360